A Parametric Open Circuit Voltage Model for Lithium Ion Batteries

C. R. Birkl,[a,*] E. McTurk,[b,*] M. R. Roberts,[b] P. G. Bruce,[b,**] and D. A. Howey[a,**,z]

[a]*Department of Engineering Science, University of Oxford, Oxford OX1 3PJ, United Kingdom*
[b]*Department of Materials, University of Oxford, Oxford OX1 3PH, United Kingdom*

We present an open circuit voltage (OCV) model for lithium ion (Li-ion) cells, which can be parameterized by measurements of the OCV of positive and negative electrode half-cells and a full cell. No prior knowledge of physical parameters related to particular cell chemistries is required. The OCV of the full cell is calculated from two electrode sub-models, which are comprised of additive terms that represent the phase transitions of the active electrode materials. The model structure is flexible and can be applied to any Li-ion cell chemistry. The model can account for temperature dependence and voltage hysteresis of the OCV. Fitting the model to OCV data recorded from a Li-ion cell at 0°C, 10°C, 20°C, 30°C and 40°C yielded high accuracies with errors (RMS) of less than 5 mV. The model can be used to maintain the accuracy of dynamic Li-ion cell models in battery management systems by accounting for the effects of capacity fade on the OCV. Moreover, the model provides a means to separate the cell's OCV into its constituent electrode potentials, which allows the electrodes' capacities to be tracked separately over time, providing an insight into prevalent degradation mechanisms acting on the individual electrodes.

The open circuit voltage (OCV) of lithium ion (Li-ion) cells plays a central role in battery models used in battery management systems (BMS) for a wide range of applications from consumer electronics to automotive systems. The OCV of a battery cell is the potential difference between the positive electrode (PE) and the negative electrode (NE) when no current flows and the electrode potentials are at equilibrium. A battery undergoing charge or discharge does not exhibit this potential since it is modified by kinetic effects such as mass transport. However, the OCV of a battery over the full range of states of charge can be obtained by charging or discharging the battery utilizing a galvanostatic intermittent titration technique (GITT) and measuring the potential at the end of each relaxation period (assuming the period is long enough to reach equilibrium). All dynamic battery models rely on the knowledge of the relationship between OCV and cell capacity in order to produce accurate estimates of internal battery states such as the state of charge (SOC) and the state of health (SOH). The SOC of a cell is a measure of how much charge remains within the cell relative to its maximal capacity. The SOC is generally expressed as a percentage; SOC = 100% indicates a fully charged cell and SOC = 0% a fully discharged cell. The SOH describes the performance deterioration of a cell at any point in time compared to the cell's initial performance. Two important metrics for the SOH are capacity fade and the increase in internal resistance, which relates to power fade. Capacity fade affects the OCV of a cell, which must be accounted for in dynamic cell models in a BMS, to ensure continued accuracy.

Battery models typically incorporate the OCV as a function of cell capacity or SOC by storing measured OCV values in look-up tables[1–3] or by fitting empirical functions to OCV data.[4–6] These techniques are popular due to their ease of implementation and good initial performance. However, since capacity fade affects the relationship between OCV and cell capacity as the cell degrades, dynamic cell models become increasingly inaccurate if their underlying OCV expression does not account for capacity fade. Although capacity fade can theoretically be estimated in on-line systems,[7] the subtle changes in the shape of the OCV curve that occur as a result of degradation are usually not considered. These changes in OCV contain valuable information about the SOH of the electrodes and, consequently, the cell.[8–10]

Physical OCV models incorporate thermodynamic information about the positive[11–13] and the negative[14] electrode materials, such as the number and types of phase transitions undergone by the electrode materials during charge and discharge and the amount of lithium that is intercalated in any given phase. Tracking these electrode characteristics throughout the cell's life would help identify predominant degradation mechanisms and allow for predictions of the cell's end-of-life. Current physics-based OCV models of various electrode materials require detailed knowledge of a large number of physical model parameters which are not typically known for commercial Li-ion cells. Moreover, they are computationally complex and not easily integrated with standard dynamic battery models. There is thus a need for an OCV model with easily identifiable parameters which allows the capturing of the OCV characteristics of both electrodes and the tracking of them throughout the lifetime of the cell.

The proposed OCV model is based on additive terms that represent the phase transitions of the positive and negative electrode materials. The model structure is flexible and can be used for any Li-ion cell chemistry. The model parameters are identified by fitting the model to OCV data of electrode half-cells and full cell. No prior knowledge of physical parameters relating to particular cell chemistries is required, which makes this model particularly suitable for practical applications in battery management systems. The ability to account for capacity fade in the model can improve the accuracy of dynamic Li-ion cell models as the cell degrades over time. Furthermore, the model provides a means to separate the OCV measured on a full cell into its constituent electrode potentials. Tracking the OCV of the positive and negative electrodes facilitates the identification of prevalent degradation mechanisms acting on each electrode.

Experimental

The objective of the experiments was to accurately measure the OCV of commercial Li-ion cells and their electrodes, in order to parameterize the model. All OCV data presented in this work was collected using commercially available pouch cells or their harvested electrode materials. The obtained cells were Kokam, model SLPB 533459H, 740 mAh nominal capacity. The NE material is graphite and the PE material is $LiMO_2$ (where M = a combination of Ni, Co and Mn, commercially known as NMC). Measurements of the specific capacity of the electrode materials gave 180 ± 5 mAh/g for the PE (NMC) and 270 ± 5 mAh/g for the NE (graphite). Measurements of OCV were conducted at five different temperatures, covering the

*Electrochemical Society Student Member.
**Electrochemical Society Active Member.
[z]E-mail: david.howey@eng.ox.ac.uk

Table I. Active mass in electrode half-cells.

Test temperature	Active mass PE	Active mass NE
0°C	12.9 mg	10.6 mg
10°C	15.8 mg	10.9 mg
20°C	12.9 mg	10.7 mg
30°C	15.8 mg	10.9 mg
40°C	15.8 mg	10.6 mg

usage range recommended by the manufacturer: 0°C, 10°C, 20°C, 30°C and 40°C. At each temperature the OCV was recorded on one fresh (uncycled) full cell, one newly constructed PE half-cell and one NE half-cell. The PE and NE half-cells were fabricated in coin cell format from electrode material harvested from fresh (uncycled) Kokam pouch cells.

Electrode half-cells.— The term *half-cells* used in this work describes electrochemical cells consisting of active electrode materials (graphite in case of the NE and NMC in case of the PE) as working electrodes and lithium foil as counter electrodes, fabricated in coin cell format. Electrode material was extracted from Kokam pouch cells in an argon atmosphere inside a glove box. The pouch cell was cut open with a scalpel and samples of the PE and NE (active material on current collectors) were removed from the stack. The electrodes were cut into disks of 15 mm diameter using a hole punch, giving 1.77 cm² of active electrode areas for both the PE and the NE half-cells. In Kokam pouch cells, both sides of the PE and NE current collectors are coated with active electrode material. In order to improve the electronic conductivity between the electrode sample and the coin cell base, and to prevent a disparity in ionic transport between the side of active material that faces the separator and the side that would face away from it and be pressed up against the coin cell base, the active material was removed from one side of the current collector. This was achieved using N-Methyl-2-Pyrrolidone to dissolve the binder of the active material. Dimethyl carbonate was subsequently used to rinse the electrode before assembling the half-cell. The active mass of each electrode was measured by cutting a 15 mm disk of the current collector material (copper for the NE and aluminium for the PE) and removing the active material from both sides of the sample, as described for the half-cell electrodes above. The current collector samples were weighed and their mass was subtracted from the total mass of each half-cell electrode in order to determine the active mass of the half-cell electrodes (see Table I). The half-cell electrodes were placed in a coin cell base, followed by a glass microfiber separator wetted with LP30 (LiPF$_6$ solution in ethylene carbonate (EC) and dimethyl carbonate (DMC); 1.0 M LiPF$_6$ in EC/DMC = 50/50 (wt/wt)) electrolyte, lithium foil as the counter electrode, a spacer, a spring for improved contact and the coin cell lid (see Figure 1).

OCV measurements.— In this work, we apply the term *OCV* to the full cell and the electrodes alike. We define the OCV of an electrode as its equilibrium potential, whereby the electrons of both phases of
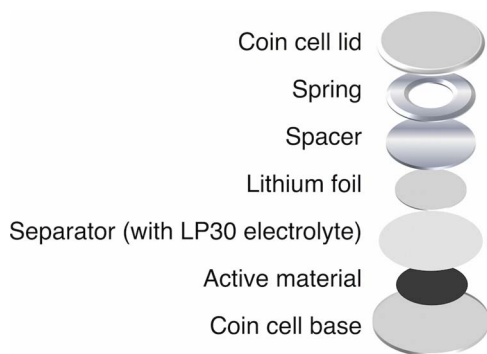
the redox couple, in our case Li/Li⁺, are in equilibrium.[15] The OCV of unmodified commercial Kokam pouch cells, PE and NE half-cells were measured at 0°C, 10°C, 20°C, 30°C and 40°C. All experiments were carried out using BioLogic SP-150 potentiostats inside a Vötsch thermal chamber to control the environmental temperature. Measurements at each temperature were recorded on fresh (uncycled) commercial Kokam cells or newly fabricated electrode half-cells. In order to obtain true OCV measurements over the entire capacity range of the full cells and half-cells, the SOC of the full cells and half-cells was changed incrementally, in steps of 1/50 of the nominal capacity ($\triangle Q = Q_{nom}/50$), by applying small currents (C/10) and subsequently allowing the cell voltage to relax for one hour. The nominal electrode half-cell capacities, Q_{nom}, were calculated based on their active masses and their known specific capacities (PE: 180 ± 5 mAh/g, NE: 270 ± 5 mAh/g). The OCV measurements were recorded at the end of each relaxation period. This method of OCV measurement is commonly referred to as galvanostatic intermittent titration technique (GITT).[16] In order to account for the voltage hysteresis commonly observed in Li-ion cells,[17–19] GITT measurements were recorded during incremental charge and discharge. Figure 2 illustrates a GITT measurement on a commercial Kokam cell recorded during incremental discharge. The recording of each GITT data set was preceded by a thermal equilibration period of >3 h at the respective test temperature and a subsequent constant current constant voltage (CCCV) charge. The exact experimental procedures for the GITT tests and preceding charge steps on full cell and half-cells are given in Table II.

In order to ensure that the OCV measurements of the electrode half-cells are not affected by rapid capacity fade, PE and NE half-cell capacities were recorded during five cycles (GITT during incremental discharge and charge) at 40°C (see Figure 3). The capacity fade of
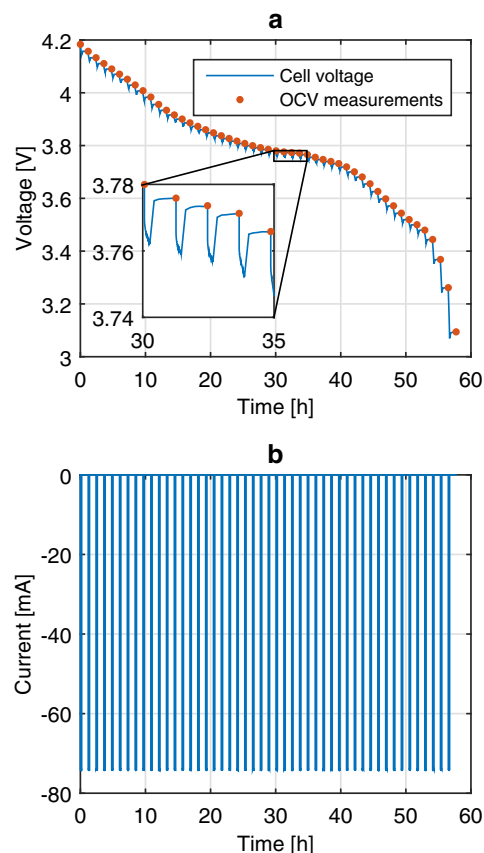
Figure 2. Illustration of GITT recorded on a 740 mAh Kokam pouch cell at 40°C by incremental discharge ($\triangle Q = 74$ mAh) and subsequent relaxation. a: Cell voltage (line) and OCV measurements (markers), recorded at the end of each relaxation period. b: Current applied for incremental discharge.

Figure 1. Coin cell assembly of the electrode half-cells.

Table II. Experimental procedure for GITT tests.

Cell type	Step No	Exp. Step	Current rate	Limits
Full cell	1	Thermal equilibration	-	$t > 3$ h
	2	Constant current charge	C/10	$V > 4.2$ V
	3	Constant voltage charge	variable	$I < 40$ mA
	4	Voltage relaxation	-	$t > 3$ h
	5	Partial constant current discharge	C/10	$\triangle Q > Q_{nom}/50$
	6	Voltage relaxation	-	$t > 1$ h
	7	Repeat steps 5 and 6 until V-limit reached	-	$V < 2.7$ V
	8	Partial constant current charge	C/10	$\triangle Q > Q_{nom}/50$
	9	Voltage relaxation	-	$t > 1$ h
	10	Repeat steps 8 and 9 until V-limit reached	-	$V > 4.2$ V
PE half-cell	1	Thermal equilibration	-	$t > 3$ h
	2	Constant current charge	C/10	$V > 4.5$ V
	3	Constant voltage charge	variable	$I < 0.01$ mA
	4	Voltage relaxation	-	$t > 3$ h
	5	Partial constant current discharge	C/10	$\triangle Q > Q_{nom}/50$
	6	Voltage relaxation	-	$t > 1$ h
	7	Repeat steps 5 and 6 until V-limit reached	-	$V < 2.5$ V
	8	Partial constant current charge	C/10	$\triangle Q > Q_{nom}/50$
	9	Voltage relaxation	-	$t > 1$ h
	10	Repeat steps 8 and 9 until V-limit reached	-	$V > 4.5$ V
NE half-cell	1	Thermal equilibration	-	$t > 3$ h
	2	Constant current charge	C/10	$V > 1.25$ V
	3	Constant voltage charge	variable	$I < 0.01$ mA
	4	Voltage relaxation	-	$t > 3$ h
	5	Partial constant current discharge	C/10	$\triangle Q > Q_{nom}/50$
	6	Voltage relaxation	-	$t > 1$ h
	7	Repeat steps 5 and 6 until V-limit reached	-	$V < 0.001$ V
	8	Partial constant current charge	C/10	$\triangle Q > Q_{nom}/50$
	9	Voltage relaxation	-	$t > 1$ h
	10	Repeat steps 8 and 9 until V-limit reached	-	$V > 1.25$ V
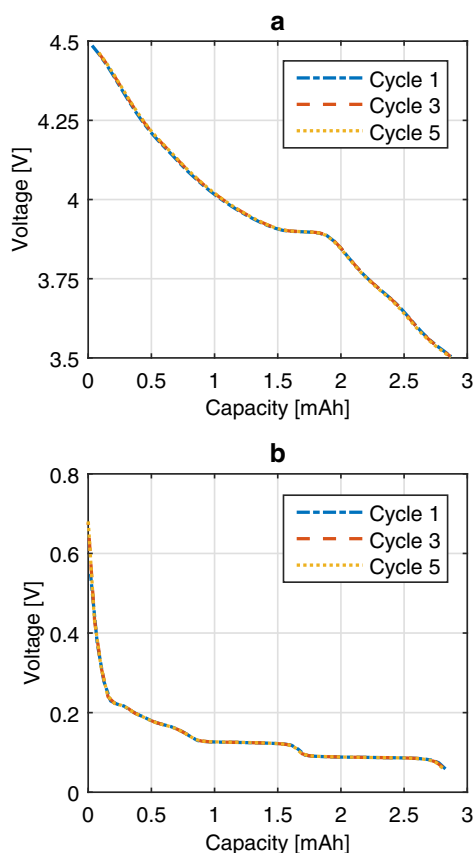
Figure 3. OCV as a function of discharged capacity of PE (a) and NE (b) half-cells recorded at 40°C over 5 discharge/charge cycles. Incremental discharge of the electrodes corresponds to lithiation of the active materials.

both PE and NE half-cells was <0.1% of their initial capacity after the first cycle and <1% after five cycles.

Modeling

Electrode sub-models.— We start by formulating the chemical potential μ of intercalated ions. The chemical potential determines the change in internal energy resulting from a change in the concentration of the ionic species.[20] The chemical potential at equilibrium can be calculated using the Nernst equation:[11]

$$\mu = E_0 - kT \ \ln\left[\frac{x}{1-x}\right] \tag{1}$$

where E_0 is the standard redox potential, k is the Boltzmann constant, T is the temperature and x is the ratio of intercalated sites to available sites in the host structure. In intercalation reactions, E_0 reflects the energy of an intercalated ion on a specific site in the lattice of the host material. Not all lattice sites have the same energies in insertion compounds and each type of lattice site hosts a limited number of ions.[21] Equation 1 therefore needs to be extended to account for N different site energies $E_{0,i}$, (where $i = \{1, 2, \ldots, N\}$) and the respective fraction of occupied sites x. McKinnon and Haering[11] reformulated Equation 1 so that it can be expressed for multiple $E_{0,i}$ according to

$$x = \frac{1}{1 + \exp^{(E_0 - \mu)/kT}} \tag{2}$$

which is also referred to as Fermi-Dirac distribution.[22] Equation 2 can be used to calculate the fraction of occupied sites in a system of N different site energies as a function of the chemical potential μ according to

$$x(\mu) = \sum_{i=1}^{N} \frac{\Delta x_i}{1 + \exp^{(E_{0,i} - \mu)/kT}} \tag{3}$$

where Δx_i is the fraction of occupied sites of energy $E_{0,i}$. Equations 1 to 3 have been applied by McKinnon and Haering in Ref. 11 in their discussion of lattice gas models for intercalation systems. However, this approach is limited to the particular case where intercalated ions do not interact with each other. In real systems, interactions between intercalated ions cannot be neglected. Such interactions are associated with an interaction energy U_i. In order to account for the short-range interactions between γ neighboring ions in a host lattice, Ohzuku and Ueda[12] extended Equation 1 to

$$\mu(x_i) = E_{0,i} - \gamma U_i(1 - 2x_i) - kT \ \ln\left[\frac{x_i}{1 - x_i}\right] \quad [4]$$

which gives the chemical potential as a function of occupied lattice sites of energy $E_{0,i}$. Rearranging Equation 4 to give $x(\mu)$ for multiple energy levels $E_{0,i}$ of a typical intercalation material yields impractically complex solutions. We therefore introduce a dimensionless parameter a_i in order to approximate the effects of interaction energies and substitute the term $\gamma U_i(1 - 2x_i)$ in Equation 4 by extending Equation 3 to

$$x(\mu) = \sum_{i=1}^{N} \frac{\Delta x_i}{1 + \exp^{(E_{0,i} - \mu)a_i/kT}} \quad [5]$$

The chemical potential μ is related to the open circuit voltage E^{OC} by

$$E^{OC} = -\frac{1}{ze}\mu(x_i) \quad [6]$$

where z is the number of electrons exchanged in the redox reaction ($z = 1$ for Li-ion systems) and e is the elementary charge. Combining Equations 5 and 6 gives

$$x\left(E^{OC}\right) = \sum_{i=1}^{N} \frac{\Delta x_i}{1 + \exp^{(E^{OC} - E_{0,i})a_i e/kT}} \quad [7]$$

where E^{OC} and $E_{0,i}$ are in Volts. We evaluate Equation 7 with $N = 1$ by comparing its results to those computed using Equation 4 for a range of interaction energies $-0.4\ V\ <\ \gamma U_i e^{-1} < 0.07\ V$ (multiplying by the elementary charge e to convert from Joules to Volts). Optimal values for parameter a_i are obtained by fitting Equation 7 to the results of Equation 4 computed for each interaction energy by minimizing the root-mean-squared error (RMSE) on $E^{OC}(x)$ using nonlinear least squares fitting in Matlab. Figure 4a shows the comparison of $E^{OC}(x) - E_0$ calculated with Equations 4 and 7, respectively, for different interaction energies. The RMSE on $E^{OC}(x)$ is plotted against a range of $\gamma U_i e^{-1}$ in Figure 4b, alongside the relationship between a_i and $\gamma U_i e^{-1}$. The approximation of the term $\gamma U_i e^{-1}(1 - 2x_i)$ by parameter a_i is obviously best close to $\gamma U_i e^{-1} = 0$, where Equations 4 and 7 are identical. The discrepancy between $E^{OC}(\gamma U_i e^{-1}, x)$ and $E^{OC}(a_i, x)$ increases for increasingly smaller or larger values of $\gamma U_i e^{-1}$. Figure 4a shows that for large positive values of $\gamma U_i e^{-1}$, the voltage can rise with x_{Li} according to Equation 4, which is considered unphysical.[11] This behavior cannot be modeled with Equation 7, which is limited by a constant voltage profile for large absolute values of parameter a_i (see Figure 4a: $E^{OC}(|a|_{max}, x)$).

The comparison of $E^{OC}(\gamma U_i e^{-1}, x)$ and $E^{OC}(a_i, x)$ shows that Equation 7 gives a good approximation of Equation 4 for a wide range of interaction energies. More importantly, Equation 7 enables us to calculate the OCV for multiple site energies, as are encountered in real intercalation electrode materials. Equation 7 is therefore selected as the basis for the electrode sub-models for the PE (NMC) and the NE (graphite).

It should be emphasized at this stage that the objective of this work is not to derive a model for intercalation electrodes from first principles but to build upon established principles (outlined in Equations 1 to 4) in order to create an OCV model for commercial Li-ion cells, which can be identified without prior knowledge of physical parameters of the active electrode materials, and used in a BMS. The first step in the model identification process is to estimate the number of phase
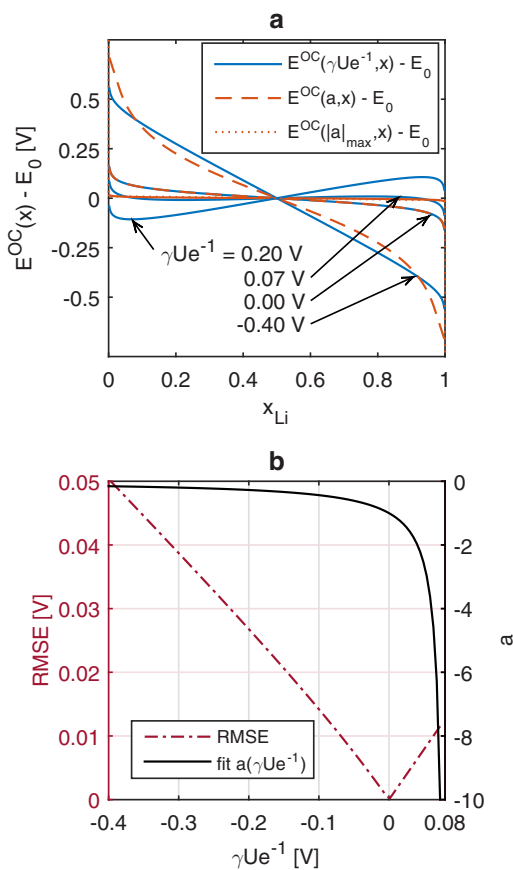

Figure 4. a: Comparison of $E^{OC}(x) - E_0$ computed by Equation 4 (solid line) and Equation 7 (broken line), respectively for various values of $\gamma U_i e^{-1}$. b (left axis, broken line): RMSE on $E^{OC}(x)$ from fitting Equation 7 to Equation 4. b (right axis, solid line): Correlation between parameter a_i and $\gamma U_i e^{-1}$.

transitions that each electrode material undergoes during charge and discharge. Phase transitions can be identified by plateaus in the voltage curves of the half-cells. Since it can be difficult to identify these plateaus in curves of voltage versus capacity, we first differentiate half-cell capacity Q with respect to voltage V (dQ/dV) in order to obtain more clearly visible peaks.[23] This is illustrated in Figure 5, where the voltages of the PE and NE half-cells, recorded at $20°$C, are shown in the top row (Figure 5a and 5b) and the respective dQ/dV curves are in the bottom row (Figure 5c and 5d). This analysis indicates that there are four identifiable phases transitions ($N = 4$) in both positive and negative electrode material, which leads to the PE and NE OCV model equations

$$x_{PE}\left(E_{PE}^{OC}\right) = \sum_{i=1}^{4} \frac{\Delta x_{PE,i}}{1 + \exp^{(E_{PE}^{OC} - E_{0,PE,i})a_{PE,i}e/kT}} \quad [8]$$

$$x_{NE}\left(E_{NE}^{OC}\right) = \sum_{i=1}^{4} \frac{\Delta x_{NE,i}}{1 + \exp^{(E_{NE}^{OC} - E_{0,NE,i})a_{NE,i}e/kT}} \quad [9]$$

It should be noted that these equations are intended to capture the observable phase transitions in the active electrode materials, which may not be equivalent to the actual total number of phase transitions that the materials undergo, but is nonetheless still useful for diagnostic and fitting purposes.

Given the voltage ranges of $\mathbf{E}_{PE}^{OC}$ and $\mathbf{E}_{NE}^{OC}$ (which are vectors of equally spaced elements ranging from the minimum to the maximum electrode voltage), Equations 8 and 9 are used to determine the ratio of occupied to available sites in the electrode materials for all identified phase transitions $i = \{1, 2 \ldots 4\}$. To calculate this, three parameters
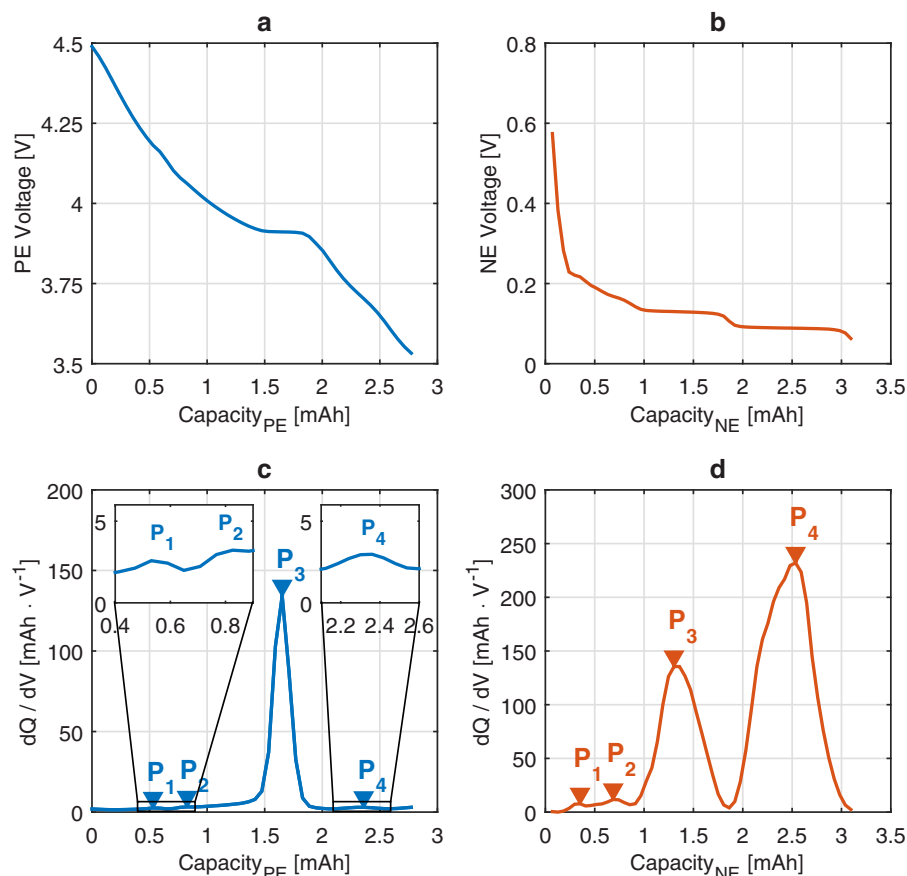
Figure 5. a: PE half-cell voltage, b: NE half-cell voltage, c: dQ/dV of PE versus capacity. d: dQ/dV of NE versus capacity. Electrode capacity corresponds to intercalated lithium. Electrode processes P_i are numbered from the highest to the lowest potential $E_{0,i}$.

Δx_i, $E_{0,i}$ and a_i must be estimated. For a cell model consisting of two electrode sub-models with four phase transitions in each electrode, a total of 24 parameters are required.

The cell model.— The OCV model is composed of three parts (illustrated in Figure 6):

1. Determination of utilized electrode capacity range

Figure 6. OCV model schematic.

2. Calculation of electrode voltages (electrode sub-models)
3. Calculation of cell voltage

Since Equations 8 and 9 give the lithium content of each electrode as a function of electrode potential, they must be solved iteratively to yield $\hat{E}_{PE}^{OC}(\hat{x}_{PE,cell})$ and $\hat{E}_{NE}^{OC}(\hat{x}_{NE,cell})$, where $\hat{x}_{PE,cell}$ and $\hat{x}_{NE,cell}$ are vectors, describing the estimated capacity ranges of the positive and negative electrode respectively that are utilized inside a full cell. The OCV of the full cell is subsequently calculated based on the half-cell OCVs of the PE and the NE according to

$$E_{Cell}^{OC} = E_{PE}^{OC} - E_{NE}^{OC}. \qquad [10]$$

Parameter estimation.— The proposed OCV model requires the estimation of the upper and lower limits of the PE and NE capacity ranges utilized within the full cells as well as 24 parameters for the electrode sub-models: Δx_i, $E_{0,i}$ and a_i for each of the four phase transitions identified in the NMC material of the PE and the graphite in the NE. All parameters are estimated using Matlab's constrained optimization function *fmincon*. The cost functions and associated parameters are listed in Table III. The parameter estimation procedure consists of three steps:

1. Estimation of the useful electrode capacity ranges.
   $\mathbf{x}_{Cell}$, $\mathbf{x}_{PE}$ and $\mathbf{x}_{NE}$ are vectors of measured SOC of the full cell, PE half-cell and NE half-cell respectively. Each element in these SOC vectors is associated with a measurement of OCV, comprising the vectors $\mathbf{E}_{Cell}^{OC}$, $\mathbf{E}_{PE}^{OC}$, and $\mathbf{E}_{NE}^{OC}$ for the OCV of the cell, the PE half-cell and the NE half-cell, respectively. $\hat{x}_{PE}$ and $\hat{x}_{NE}$ are vectors of the estimated SOC ranges of the PE and the NE, which are utilized within a full cell. $\hat{x}_{PE}$ and $\hat{x}_{NE}$ are subsets of the vectors $\mathbf{x}_{PE}$ and $\mathbf{x}_{NE}$ measured in half-cells because not the entire capacity range of the half-cells is utilized in a full cell due to the
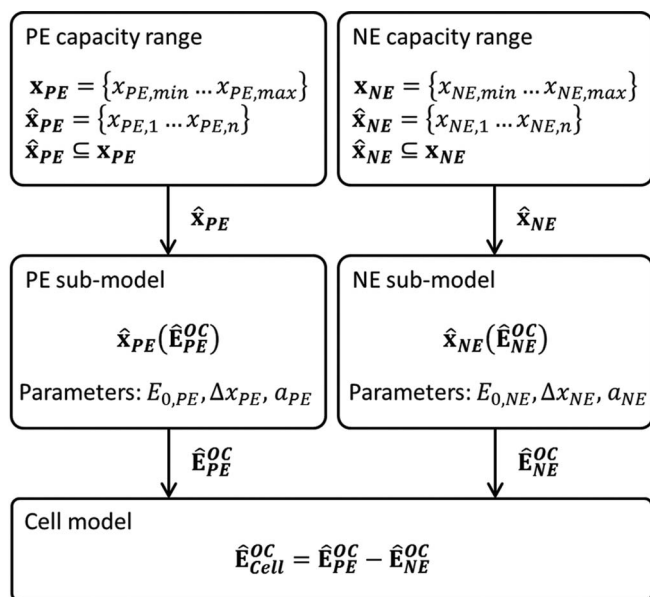
Table III. Summary of parameter estimation.

Capacity range estimation

$$\arg_{\theta_x} \min \text{RMSE} = \sqrt{\frac{\sum_{i=1}^n (\hat{\mathbf{x}}_{Cell,i}(\theta_x) - \mathbf{x}_{Cell})^2}{n}} \quad [11]$$

$\mathbf{x}_{Cell} = \{x_{Cell,min} \ldots x_{Cell,max}\}$
$\mathbf{x}_{PE} = \{x_{PE,min} \ldots x_{PE,max}\}$
$\mathbf{x}_{NE} = \{x_{NE,min} \ldots x_{NE,max}\}$
$\hat{\mathbf{x}}_{PE} = \{x_{PE,1} \ldots x_{PE,n}\}$
$\hat{\mathbf{x}}_{PE} \subseteq \mathbf{x}_{PE}$
$\hat{\mathbf{x}}_{NE} = \{x_{NE,1} \ldots x_{NE,n}\}$
$\hat{\mathbf{x}}_{NE} \subseteq \mathbf{x}_{NE}$
$\mathbf{E}_{Cell}^{OC} = \{E_{Cell,min}^{OC} \ldots E_{Cell,max}^{OC}\}$
$\hat{\mathbf{E}}_{Cell}^{OC}(\hat{\mathbf{x}}_{Cell}) = \hat{\mathbf{E}}_{PE}^{OC}(\hat{\mathbf{x}}_{PE}) - \hat{\mathbf{E}}_{NE}^{OC}(\hat{\mathbf{x}}_{NE})$
$\theta_x = \begin{bmatrix} x_{PE,1} & x_{NE,1} \\ x_{PE,n} & x_{NE,n} \end{bmatrix}$

Estimates for initial guess of parameters $E_{0,PE}$, Δx_{PE}, a_{PE}

$$\arg_{\theta_{PE}} \min \text{RMSE} = \sqrt{\frac{\sum_{i=1}^n (\hat{\mathbf{E}}_{PE,i}^{OC}(\theta_{PE}) - \mathbf{E}_{PE}^{OC})^2}{n}} \quad [12]$$

$\mathbf{E}_{PE}^{OC} = \{E_{PE,min}^{OC} \ldots E_{PE,max}^{OC}\}$

$$\theta_{PE} = \begin{bmatrix} E_{0,PE,1} & \Delta x_{PE,1} & a_{PE,1} \\ E_{0,PE,2} & \Delta x_{PE,2} & a_{PE,2} \\ \vdots & \vdots & \vdots \\ E_{0,PE,4} & \Delta x_{PE,4} & a_{PE,4} \end{bmatrix}$$

Estimates for initial guess of parameters $E_{0,NE}$, Δx_{NE}, a_{NE}

$$\arg_{\theta_{NE}} \min \text{RMSE} = \sqrt{\frac{\sum_{i=1}^n (\hat{\mathbf{E}}_{NE,i}^{OC}(\theta_{NE}) - \mathbf{E}_{NE}^{OC})^2}{n}} \quad [13]$$

$\mathbf{E}_{NE}^{OC} = \{E_{NE,min}^{OC} \ldots E_{NE,max}^{OC}\}$

$$\theta_{NE} = \begin{bmatrix} E_{0,NE,1} & \Delta x_{NE,1} & a_{NE,1} \\ E_{0,NE,2} & \Delta x_{NE,2} & a_{NE,2} \\ \vdots & \vdots & \vdots \\ E_{0,NE,4} & \Delta x_{NE,4} & a_{NE,4} \end{bmatrix}$$

Parameter estimation for cell model

$$\arg_{\theta_{Cell}} \min \text{RMSE} = \sqrt{\frac{\sum_{i=1}^n (\hat{\mathbf{E}}_{Cell,i}^{OC}(\theta_{Cell}) - \mathbf{E}_{Cell}^{OC})^2}{n}}$$
$$+ \sqrt{\frac{\sum_{i=1}^n (\hat{\mathbf{E}}_{PE,i}^{OC}(\theta_{PE}) - \mathbf{E}_{PE}^{OC})^2}{n}}$$
$$+ \sqrt{\frac{\sum_{i=1}^n (\hat{\mathbf{E}}_{NE,i}^{OC}(\theta_{NE}) - \mathbf{E}_{NE}^{OC})^2}{n}} \quad [14]$$

$\mathbf{E}_{Cell}^{OC} = \{E_{Cell,min}^{OC} \ldots E_{Cell,max}^{OC}\}$
$\hat{\mathbf{E}}_{Cell}^{OC} = \hat{\mathbf{E}}_{PE}^{OC} - \hat{\mathbf{E}}_{NE}^{OC}$

$$\theta_{Cell} = \begin{bmatrix} E_{0,PE,1} & \Delta x_{PE,1} & a_{PE,1} & E_{0,NE,1} & \Delta x_{NE,1} & a_{NE,1} \\ E_{0,PE,2} & \Delta x_{PE,2} & a_{PE,2} & E_{0,NE,2} & \Delta x_{NE,2} & a_{NE,2} \\ \vdots & \vdots & \vdots & \vdots & \vdots & \vdots \\ E_{0,PE,4} & \Delta x_{PE,4} & a_{PE,4} & E_{0,NE,4} & \Delta x_{NE,4} & a_{NE,4} \end{bmatrix}$$

different upper and lower voltage limits imposed on a full cell during OCV measurements. $\hat{\mathbf{x}}_{PE}$ and $\hat{\mathbf{x}}_{NE}$ must therefore be estimated by comparing the associated OCV of the PE, $\hat{\mathbf{E}}_{PE}^{OC}(\hat{\mathbf{x}}_{PE})$, and the NE, $\hat{\mathbf{E}}_{NE}^{OC}(\hat{\mathbf{x}}_{NE})$, and the resulting estimated cell OCV, $\hat{\mathbf{E}}_{Cell}^{OC}(\hat{\mathbf{x}}_{Cell})$, to the measured cell OCV, $\mathbf{E}_{Cell}^{OC}(\mathbf{x}_{Cell})$. This is achieved by optimization using the objective function given in Table III, Equation 11, which varies the parameters $x_{PE/NE,1}$ and $x_{PE/NE,n}$ (summarized in matrix θ_x) in order to minimize the RMSE between $\mathbf{x}_{Cell}$ and $\hat{\mathbf{x}}_{Cell}$.

2. Estimation of initial guesses for electrode sub-model parameters:
    a. PE parameters $E_{0,PE,i}$, $\Delta x_{PE,i}$ and $a_{PE,i}$ for phase transitions i, where $i = \{1, 2 \ldots 4\}$. The PE parameters are summarized in a 3 by 4 matrix θ_{PE} and calculated by minimizing the RMSE between the estimated and the measured OCV of the PE, $\hat{\mathbf{E}}_{PE}^{OC}(\theta_{PE})$ and $\mathbf{E}_{PE}^{OC}$, respectively. This is achieved by an optimization using the objective function given in Table III, Equation 12. $\hat{\mathbf{E}}_{PE}^{OC}(\theta_{PE})$ is calculated using Equation 8.

    b. NE parameters $E_{0,NE,i}$, $\Delta x_{NE,i}$ and $a_{NE,i}$ for phase transitions i, where $i = \{1, 2 \ldots 4\}$. The NE parameters are summarized in a 3 by 4 matrix θ_{NE} and calculated by minimizing the RMSE between the estimated and the measured OCV of the NE, $\hat{\mathbf{E}}_{NE}^{OC}(\theta_{NE})$ and $\mathbf{E}_{NE}^{OC}$, respectively. This is achieved by an optimization using the objective function given in Table III, Equation 13. $\hat{\mathbf{E}}_{NE}^{OC}(\theta_{NE})$ is calculated using Equation 9.

3. Combined estimation of parameters $E_{0,i}$, Δx_i and a_i in both PE and NE using initial parameter estimates obtained in steps 1 and 2.

    The estimated electrode capacity ranges obtained in step 1 and the initial parameter guesses obtained in step 2 are used to initiate the simultaneous estimation of the PE and NE parameters for the full cell model, summarized in matrix θ_{Cell}. This is achieved by minimizing the sum of RMSE between the estimated and measured OCV of the cell, the PE half-cell and the NE half-cell, as given by Equation 14 in Table III.

Results and Discussion

Hysteresis in OCV measurements.— A small voltage gap or hysteresis between charging and discharging OCV curves is present even when using a technique such as GITT where measurements are taken when no current flows and the cell has returned to its equilibrium potential. This phenomenon has been described in the literature for many common electrode materials used in Li-ion cells, such as graphite,[24] LiMnO$_2$[17] and LiCoO$_2$[25] and was also observed with the NMC cells used in this work (see Figure 7). Moreover, the magnitude and shape of the voltage hysteresis is temperature dependent in the case of the analyzed cell type and chemistry. Figure 7 illustrates the voltage hysteresis observed between OCV measurements recorded during incremental charge (solid line) and discharge (broken line) in PE (a, b), NE (c, d)
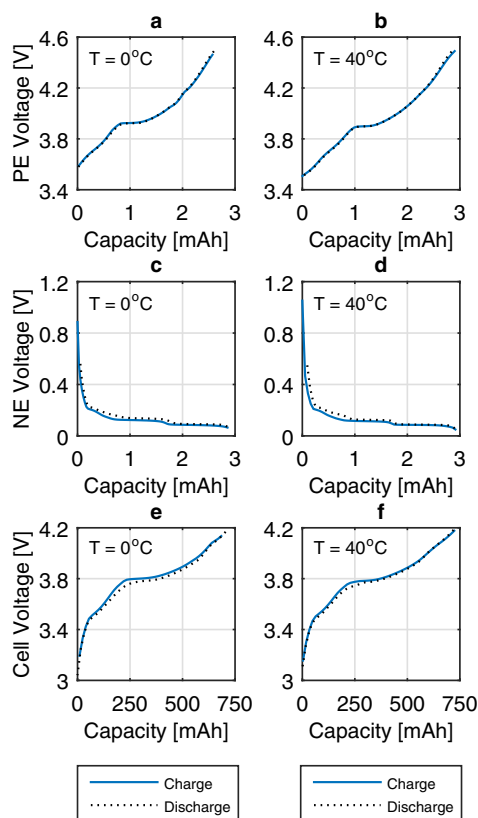

Figure 7. OCV recorded during incremental charge (solid line) and discharge (broken line) of PE (a, b), NE (c, d) and full cell (e, f) at T = 0°C (a, c, e) and T = 40°C (b, d, f).
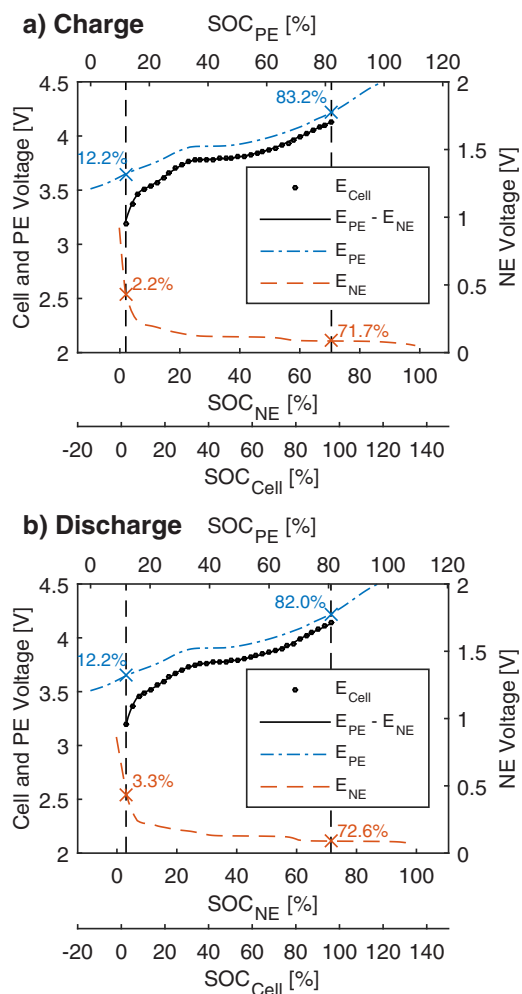
Figure 8. Results of electrode capacity range fitting to determine $\hat{\mathbf{x}}_{PE}$ and $\hat{\mathbf{x}}_{NE}$. The data were recorded using GITT at 30°C on a PE and NE half-cell and a 740 mAh commercial NMC cell during a) incremental charge and b) incremental discharge.

Figure 9. Results of electrode OCV fitting for a: PE and b: NE. Data were recorded using GITT at 20°C on a PE and NE half-cell cell, respectively, and averaged between incremental charge and discharge data. The SOC refers to the state of lithiation of the half-cells.

and full cell (e, f). OCV measurements displayed in the left column in Figures 7a, 7c, and 7e) were recorded at T = 0°C and those in the right column (Figures 7b, 7d and 7f) at T = 40°C. Voltage hysteresis is clearly observable in the full cell (Figures 7e and 7f) and appears to be largely due to the NE (Figures 7c and 7d). The maximum hysteresis observed in the full cell is on the order of 46 mV at 0°C and 33 mV at 40°C. The effects of hysteresis in Li-ion NMC cells can therefore not be ignored in an OCV model if accuracies greater than 46 mV are to be achieved. Due to the dependency of the measured OCV of the cell and half-cells on temperature and hysteresis, the parameters of the presented OCV model are estimated for both OCV measurements obtained during incremental charge and discharge at 0°C, 10°C, 20°C, 30°C and 40°C.

Estimation results for electrode capacity ranges.— Exemplary results of the estimation of the PE and NE capacity ranges are displayed in Figure 8. The measurements were recorded using GITT with incremental charge (Figure 8a) and discharge steps (Figure 8b). $\hat{\mathbf{E}}_{PE}^{OC}$ is plotted against $\hat{\mathbf{x}}_{PE}$, $\hat{\mathbf{E}}_{NE}^{OC}$ against $\hat{\mathbf{x}}_{NE}$ and $\hat{\mathbf{E}}_{Cell}^{OC}$ (calculated according to Equation 10) against $\hat{\mathbf{x}}_{Cell}$ (solid line). $\mathbf{E}_{Cell}^{OC}$ is plotted against $\mathbf{x}_{Cell}$ (markers) for comparison with $\hat{\mathbf{E}}_{Cell}^{OC}$. By estimating $\hat{\mathbf{x}}_{PE}$ and $\hat{\mathbf{x}}_{NE}$, accurate estimates of the cell OCV $\hat{\mathbf{E}}_{Cell}^{OC}$ are achieved, with RMSE < 1 mV for both charge and discharge data sets. The identified electrode capacity limits, $x_{PE,1}$, $x_{NE,1}$ and $x_{PE,n}$, $x_{NE,n}$, are displayed in the
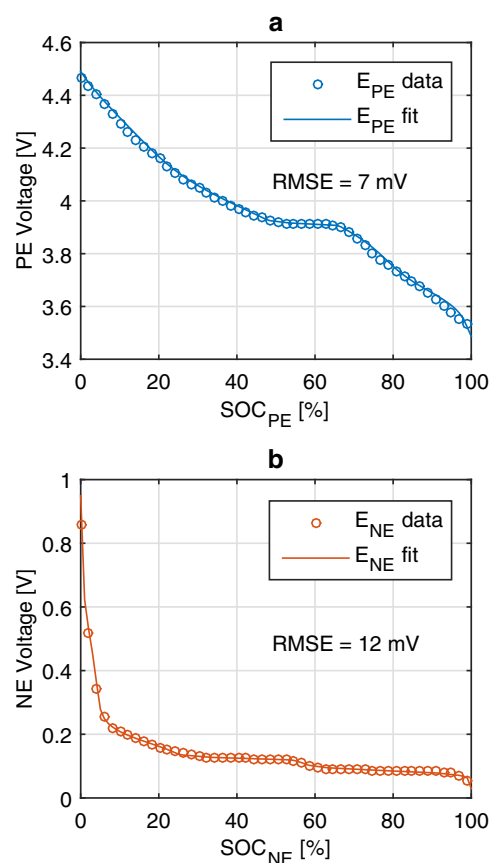
figure, marked by vertical dashed lines. The small RMSE values and the consistency of the identified capacity limits obtained for the PE and NE for the charge and discharge data confirm the validity of the fitting technique.

Estimation results for initial electrode parameter guess.— Figure 9a shows exemplary results of fitting $\hat{\mathbf{E}}_{PE}^{OC}(\theta_{PE})$ to $\mathbf{E}_{PE}^{OC}$ in order to obtain θ_{PE}. Figure 9b shows exemplary results of fitting $\hat{\mathbf{E}}_{NE}^{OC}(\theta_{PE})$ to $\mathbf{E}_{NE}^{OC}$ in order to obtain θ_{NE}. The OCV data displayed in Figure 9 is the mean of incremental charge and discharge data recorded on PE and NE half-cells at 20°C. The estimation procedure was carried out for OCV data recorded at 0°C, 10°C, 20°C, 30°C and 40°C. RMSE between $\hat{\mathbf{E}}_{PE}^{OC}$ and $\mathbf{E}_{PE}^{OC}$, and $\hat{\mathbf{E}}_{NE}^{OC}$ and $\mathbf{E}_{NE}^{OC}$ did not exceed 15 mV.

Combined estimation of PE and NE parameters for the cell model.— Figure 10 shows exemplary results of fitting the estimated OCV of the cell, $\hat{\mathbf{E}}_{Cell}^{OC}$ (solid line) to the measured OCV of the cell, $\mathbf{E}_{Cell}^{OC}$ (circular markers) at 0°C, 20°C and 40°C, for incremental charge and discharge. Figure 10 also shows the estimated OCV of the PE, $\hat{\mathbf{E}}_{PE}^{OC}$, and NE, $\hat{\mathbf{E}}_{NE}^{OC}$, comprising $\hat{\mathbf{E}}_{Cell}^{OC}$, as well as the measured OCV of the PE and NE half-cells $\mathbf{E}_{PE}^{OC}$ (diamond markers) and $\mathbf{E}_{NE}^{OC}$ (triangular markers). The estimation procedure was carried out for OCV data recorded at 0°C, 10°C, 20°C, 30°C and 40°C. RMSE and maximal errors for $\hat{\mathbf{E}}_{PE}^{OC}$, $\hat{\mathbf{E}}_{NE}^{OC}$, and $\hat{\mathbf{E}}_{Cell}^{OC}$ are given in Table IV. RMSE values did not exceed 5 mV and maximal errors did not exceed 22 mV for all fits, which indicates that the model is well suited for a temperature range between 0°C and 40°C and for both charging and discharging OCV. Figure 11 shows the residuals of the OCV fits for the full cells,
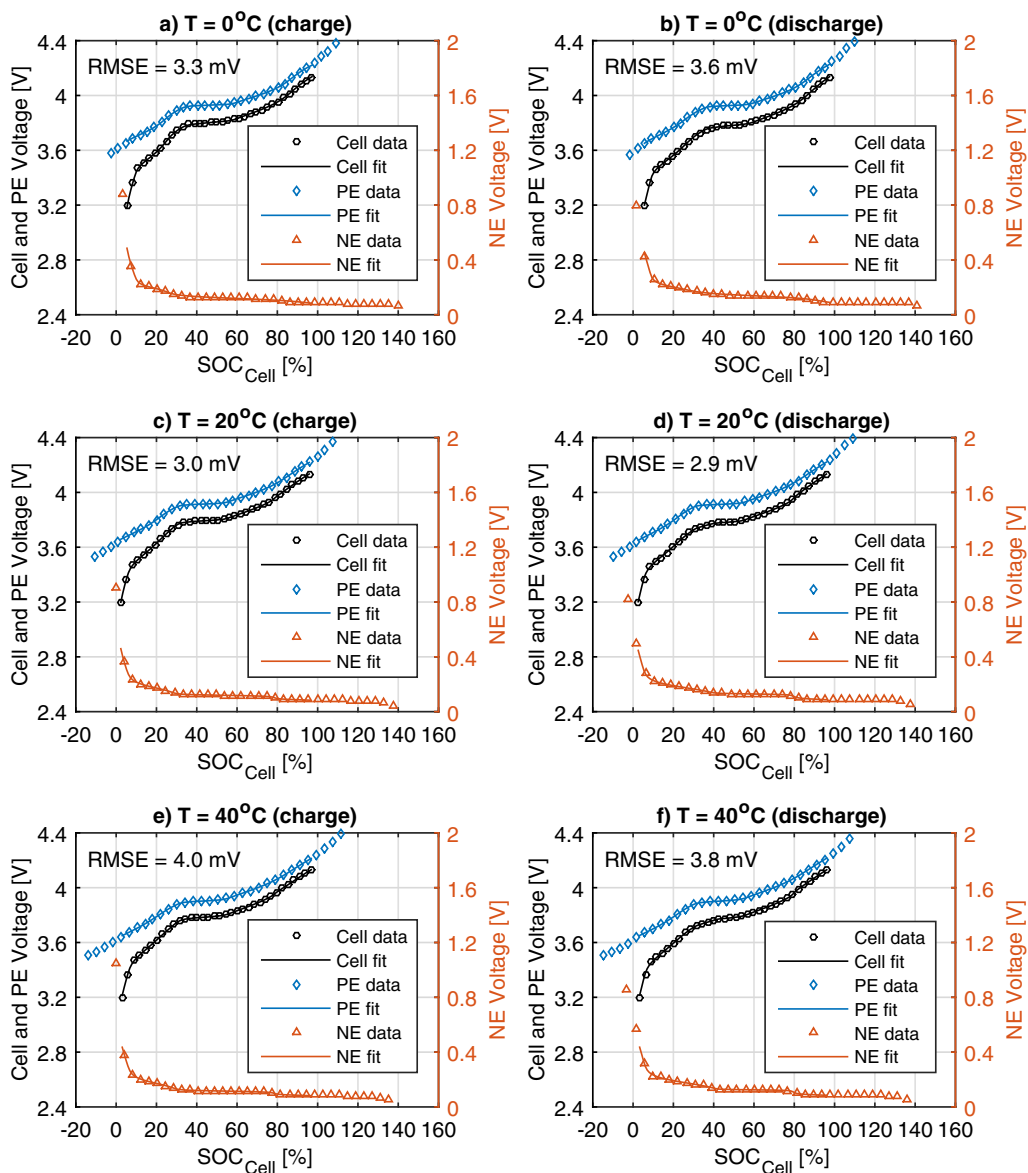
Figure 10. Fitting results of cell and electrode OCV at 0°C: a) charge b) discharge, at 20°C: c) charge, d) discharge and 40°C: e) charge, f) discharge. OCV measurements were obtained by GITT with charge and discharge increments. One fresh 740 mAh NMC cell and one set of PE and NE half-cells were used for each temperature.

the PE half-cells and the NE half-cells as a function of SOC, which demonstrates that the fitting errors do not exceed 10 mV for a cell SOC greater than 10%. The high fitting accuracies for the OCV of both the full cell and the electrode half-cells, achieved in the combined fitting procedure, shows that the integrity of the electrode sub-models is maintained in the full cell model. This is an important feature when

using the presented OCV model to track changes in the OCV of the electrodes, as cells degrade.

Figure 12 shows the results for the estimated parameters $E_{0,i}$, $\gamma U_i e^{-1}$ and Δx_i as a function of temperature and hysteresis. The indices of the parameters are consistent with those introduced in Figure 5 for the identified phase transitions in the electrode materials.

Table IV. Fitting errors of combined parameter estimation.

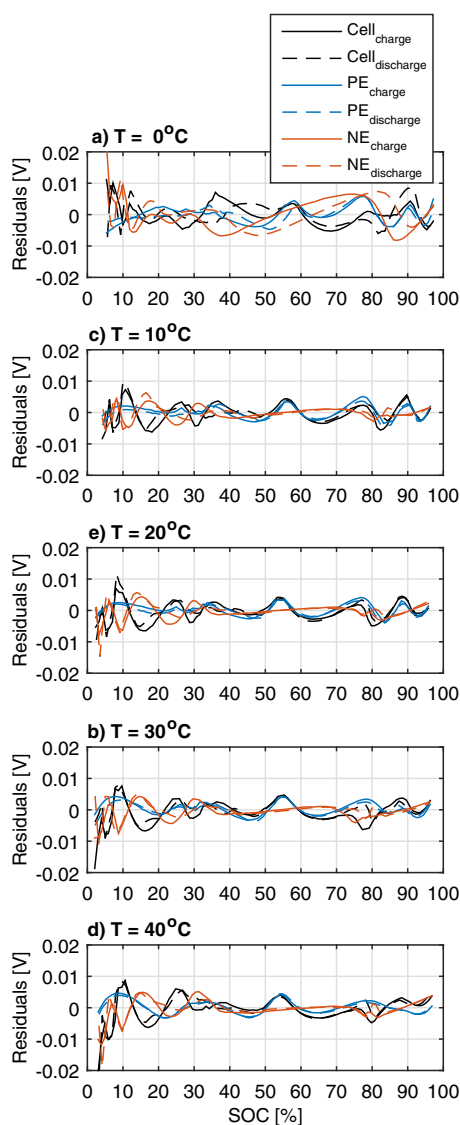|	Cell			Positive Electrode			Negative Electrode		
Temp. [°C]	RMSE$_{ch}$ [mV]	RMSE$_{dc}$ [mV]	Max Error [mV]	RMSE$_{ch}$ [mV]	RMSE$_{dc}$ [mV]	Max Error [mV]	RMSE$_{ch}$ [mV]	RMSE$_{dc}$ [mV]	Max Error [mV]
0	3	4	11	3	2	6	5	4	22
10	3	3	9	2	2	5	2	2	6
20	3	3	12	2	2	4	2	2	15
30	4	3	19	2	2	5	3	2	11
40	4	4	22	2	2	5	3	3	19

Figure 11. Residuals of OCV fits of the full cells, the PE half-cells and the NE half-cells for the combined parameter estimation at different temperatures.

The temperature dependence of PE parameters is mostly reflected by a slight increase in parameter $\Delta x_{PE,4}$, while all other parameters Δx_{PE} decrease for the PE. Parameter $\Delta x_{PE,4}$ represents high levels of lithiation in the PE. A relative increase in this parameter compared to the remaining parameters $\Delta x_{PE,i}$ indicates that more lithium is inserted into the PE during discharge of the cell at higher temperatures, which is expected.[26] The temperature dependence of the NE parameters is mostly captured by the increase of parameter $E_{0,NE,1}$ and $\gamma U_{NE,1}e^{-1}$. Moreover, it is worth noting that parameter $\Delta x_{NE,2}$ increases with temperature, while parameter $\Delta x_{NE,3}$ decreases. This indicates a shift in the utilization of the capacity ranges associated with parameters $\Delta x_{NE,2}$ and $\Delta x_{NE,3}$.

Hysteresis effects are very limited for the PE, as already observed from the raw OCV data. Most of the hysteresis is attributed to low levels of lithiation in the PE, as indicated by parameter $\Delta x_{PE,1}$, which is larger for OCV recorded during incremental charge, than discharge (see Figure 12). More pronounced effects can be observed for the NE, most notably reflected by higher values of parameter $E_{0,NE,1}$ during incremental discharge compared to charge.[24,27] Further slight hysteresis dependence can be observed for parameter $\gamma U_{NE,1}e^{-1}$ and for parameters $\Delta x_{NE,2}$ and $\Delta x_{NE,3}$. The latter show a shift in capacity utilization between parameters $\Delta x_{NE,2}$ and $\Delta x_{NE,3}$, with parameter $\Delta x_{NE,2}$ being notably smaller during charge than during discharge, while the opposite is the case for parameter $\Delta x_{NE,3}$.

Conclusions

A novel parametric model of the OCV of Li-ion battery cells has been developed. The model captures the OCV at an electrode level, based on additive terms of the Fermi-Dirac distribution function. For the first time, a physics-based OCV model has been presented which can be identified exclusively from OCV measurements of commercial cells and electrode half-cells, without prior knowledge of model parameters.

The model parameters were estimated by fitting electrode half-cell and full cell OCV data recorded at 0°C, 10°C, 20°C, 30°C and 40°C. Analysis of the identified parameters showed relatively small temperature dependence of most parameters, which means that the influence of temperature on the OCV is largely covered by the temperature term included in the model structure, as expected. The hysteresis is mostly due to the NE, reflected by parameter $E_{0,NE,1}$ and $\gamma U_{NE,1}e^{-1}$.

The model was designed to substitute empirical expressions (e.g. polynomial fits) or look-up tables for the OCV used in dynamic Li-ion battery models for BMS applications. Using the presented OCV model for BMS applications gives the advantages of:

• A flexible model structure for both electrodes, easily adaptable to any Li-ion cell chemistry.
• Parameter estimation exclusively from OCV data of PE half-cell, NE half-cell and full cell.
• Describing the OCV with 24 parameters (eliminating the need to store a large number of OCV measurements).
• Including temperature and hysteresis dependence of the OCV.

Solid lines indicate parameters estimated for the OCV during charge and broken lines during discharge. $\gamma U_i e^{-1}$ was calculated by interpolating the numerically derived correlation between parameter a_i and $\gamma U_i e^{-1}$, as demonstrated in Figure 4b. Most of the estimated parameters show little dependence on temperature and hysteresis, which indicates scope for simplification of the temperature and hysteresis dependence of the individual parameters.
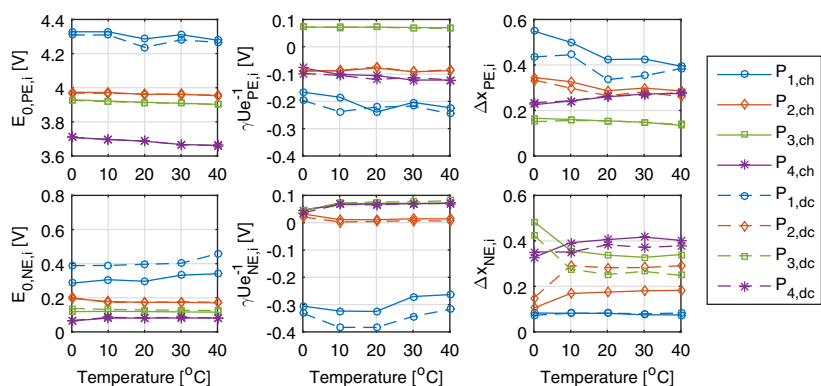

Figure 12. Parameters $E_{0,i}$, $\gamma U_i e^{-1}$ and Δx_i of PE (top row) and NE (bottom row), plotted against temperature. Solid lines indicate parameters estimated for OCV recorded during incremental charge and broken lines during incremental discharge.

• High accuracies for an operating temperature window of 0°C < T < 40°C.

• The ability to update the OCV as a function of cell capacity as the cell degrades and thereby maintaining the accuracy of the dynamic cell model for SOC estimation.

• The ability to track changes in the OCV of the electrodes as the cell degrades.

The latter point is useful to estimate the SOH of Li-ion cells on the electrode level. This can be achieved by updating the electrode-specific OCV model parameters at various stages throughout the service life of the cells. The model parameters can be updated simply by re-fitting the OCV model to OCV measurements recorded on a full cell. The changes in model parameters reveal which electrode is responsible for the capacity fade of the cell.

Future work includes the implementation of the model with a dynamic Li-ion cell model for a BMS in order to demonstrate the improved accuracies of SOC estimation throughout the cell's service life. Moreover, the OCV model will be used to diagnose electrode-specific degradation mechanisms, which can help to improve early warning systems for cell failure and extend the lifetime of Li-ion cells.

Acknowledgments

References

1. G. L. Plett, *Journal of Power Sources*, **134**, 262 (2004).
2. Y. Xing, W. He, M. Pecht, and K. L. Tsui, *Applied Energy*, **113**, 106 (2014).
3. J. Remmlinger, M. Buchholz, M. Meiler, P. Bernreuter, and K. Dietmayer, *Journal of Power Sources*, **196**, 5357 (2011).
4. Y. Hu, S. Yurkovich, Y. Guezennec, and B. J. Yurkovich, *Journal of Power Sources*, **196**, 449 (2011).
5. A. Szumanowski and Y. Chang, *IEEE Transactions on Vehicular Technology*, **57**, 1425 (2008).
6. C. Weng, J. Sun, and H. Peng, *Journal of Power Sources*, **258**, 228 (2014).
7. C. Hu, B. D. Youn, and J. Chung, *Applied Energy*, **92**, 694 (2012).
8. M. Dubarry, C. Truchot, and B. Y. Liaw, *Journal of Power Sources*, **219**, 204 (2012).
9. V. Pop et al., *Journal of The Electrochemical Society*, **154**, A744 (2007).
10. S. Wang et al., *Journal of the Electrochemical Society*, **161**, A1788 (2014).
11. W. R. McKinnon and R. R. Haering, in *Modern Aspects of Electrochemistry*, p. 235, Springer (1983).
12. T. Ohzuku and A. Ueada, *Journal of the Electrochemical Society*, **144**, 2780 (1997).
13. T. Zheng and J. Dahn, *Physical Review B*, **56**, 3800 (1997).
14. P. Derosa and P. Balbuena, *Journal of The Electrochemical Society*, **146**, 3630 (1999).
15. K. J. Vetter, *Electrochemical Kinetics - Theoretical Aspects*, p. 10, Academic Press, New York, London (1967).
16. W. Weppner and R. Huggins, *Journal of The Electrochemical Society*, **124**, 1569 (1977).
17. A. Sleigh, J. Murray, and W. McKinnon, *Electrochimica acta*, **36**, 1469 (1991).
18. J. Barker, R. Pynenburg, R. Koksbang, and M. Saidi, *Electrochimica acta*, **41**, 2481 (1996).
19. P. G. Bruce, A. R. Armstrong, and L. Gitzendammer, *Journal of Materials Chemistry*, **9**, 193 (1999).
20. E. Keszei, *Chemical Thermodynamics: An Introduction*, p. 252, Springer (2013).
21. V. V Kharton, *Solid state electrochemistry I: fundamentals, materials and their applications*, John Wiley & Sons (2009).
22. J. Honerkamp, *Statistical Physics*, 3rd ed., p. 234, Springer Berlin Heidelberg, (2012).
23. M. Dubarry, V. Svoboda, R. Hwu, and B. Yann Liaw, *Electrochemical and Solid-State Letters*, **9**, A454 (2006).
24. J. R. Dahn, T. Zheng, Y. Liu, and J. S. Xue, *Science*, **270**, 590 (1995).
25. W. Dreyer et al., *Nature materials*, **9**, 448 (2010).
26. Z. Lu, D. D. MacNeil, and J. R. Dahn, *Electrochemical and Solid-State Letters*, **4**, A191 (2001).
27. T. Ohzuku, *Journal of The Electrochemical Society*, **140**, 2490 (1993).